Zhang *et al. Biochar* (2025) 7:116
https://doi.org/10.1007/s42773-025-00522-7

Biochar

ORIGINAL RESEARCH

Open Access

Binding mechanisms of Pb(II) adsorption by biochar-derived dissolved organic matter: unraveling site heterogeneity and kinetics through advanced spectral analysis

Fuxiang Zhang[1,2†], Boyang Zhou[1,2†], Qiang Fu[1,2], Hongliang Jia[3], Yi-Fan Li[1,2,3], Yongzhen Ding[4*] and Song Cui[1,2*]

Abstract

Biochar-derived dissolved organic matter (DOM) is a highly active component that plays a critical and complex role in the immobilization of heavy metals. This study systematically investigated the impact of DOM on Pb(II) adsorption by comparing the adsorption capacities of biochar before and after DOM removal, thereby unveiling the underlying mechanisms through advanced spectroscopic techniques. Adsorption experiments demonstrated that water-washed biochar (WBC) exhibited a markedly reduced adsorption capacity (35.0 mg g^{-1}) compared to untreated biochar (BC) (96.2 mg g^{-1}), highlighting the essential role of DOM in enhancing Pb(II) adsorption. Kinetic and isothermal analyses revealed that the adsorption process was predominantly chemical in nature, as evidenced by the excellent fit of experimental data to the pseudo-second-order, Freundlich, and Temkin models. FTIR and XPS analyses confirmed that oxygen-containing functional groups, including hydroxyl, carboxyl, carbonyl, and ether groups, actively participated in Pb(II) complexation in BC, WBC, and DOM. Spectral shifts and changes in the relative abundance of C–O and C = O bonds further supported this conclusion. The Pb 4f spectra indicated that Pb(II) was primarily retained as $Pb_3(OH)_2(CO_3)_2$, with complexation identified as the dominant mechanism, followed by co-precipitation. UV differential log-transformed absorption spectra derived from titration experiments, revealed the heterogeneity of Pb(II) binding sites within DOM. Furthermore, excitation-emission matrix fluorescence spectroscopy coupled with parallel factor analysis (EEM-PARAFAC) identified three humic-like components. Among these, component C3 (humic-like and tyrosine substance) exhibited the strongest binding affinity for Pb(II). Hetero-2DCOS analysis, combined with additional spectroscopic techniques, demonstrated that carboxyl groups in humic-like substances were the most reactive sites for Pb(II) binding. These findings provide molecular-level insights into the structural and functional characteristics of biochar-derived DOM-Pb(II) complexes, offering a scientific basis for optimizing biochar-based strategies for heavy metal pollution remediation.

†Fuxiang Zhang and Boyang Zhou have authors contributed equally to this work.

*Correspondence:
Yongzhen Ding
dingyongzhen@caas.cn
Song Cui
cuisong-bq@neau.edu.cn
Full list of author information is available at the end of the article

Highlights

- Hetero-2DCOS/PARAFAC/UV-differential synergy decodes DOM-Pb(II) binding mechanisms.
- The role of biochar-derived DOM in enhancing Pb(II) adsorption was investigated.
- The UV humic-like substance (C1) reacts preferentially in humic-like components.
- Carboxyl groups in humic substances play a crucial role in DOM-Pb(II) complexation.

Keywords Biochar-derived DOM, Lead (Pb), Adsorption mechanism, Differential absorption spectra, EEM-PARAFAC, Two-dimensional correlation spectroscopy (2DCOS)

Graphical Abstract

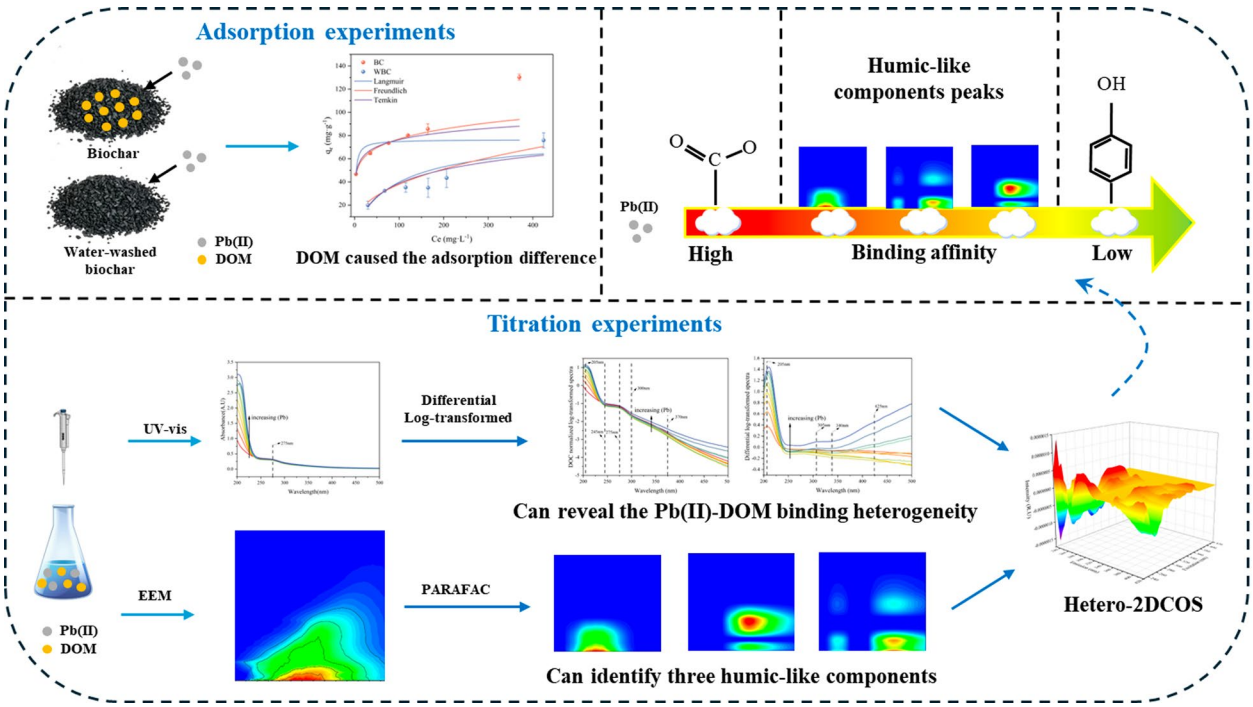

1 Introduction

Heavy metal pollution represents a critical global environmental challenge, with Pb presenting particularly severe ecological and health risks due to its toxicity, persistence, and bioaccumulation potential in ecosystems (He et al. 2012; Hou et al. 2025). Chronic exposure to Pb can lead to neurological damage, renal dysfunction, hepatic impairment (Li et al. 2014; Xu et al. 2024), underscoring the urgency of effective remediation strategies. Among various approaches, biochar, a carbon-rich material produced through pyrolysis of organic waste under oxygen-limited conditions, has garnered significant attention for its ability to immobilize heavy metals in both aqueous and soil systems (Mohan et al. 2014; Liu et al. 2018; Yang et al. 2022; Zhang et al. 2025). Its effectiveness in sequestering metals is attributed to mechanisms such as pore filling, ion exchange, surface complexation, and mineral co-precipitation, which collectively reduce the bioavailability of heavy metals (Tan et al. 2015; Nazari et al. 2019). However, during application, biochar may release dissolved organic matter (DOM), a mobile and chemically reactive component that could modify metal binding dynamics and raise concerns regarding its long-term efficacy in remediation efforts (Jiang et al. 2022).

This biochar-derived DOM is rich in oxygen-containing functional groups, such as hydroxyl, carboxyl, and phenolic moieties (Huang et al. 2020), and plays a critical

role in mediating the environmental behavior of heavy metals through mechanisms including surface complexation, electrostatic interactions, hydrogen bonding, and ion exchange (Aiken et al. 2011; Hameed et al. 2023). Notably, compared to natural DOM, biochar-derived DOM exhibits more diverse molecular characteristics and stronger affinities for metal ions, which can be attributed to structural transformations induced by pyrolysis (Yan et al. 2023). These transformations enhance the aromatic nature of DOM, as evidenced by lower H/C and O/C ratios (Yan et al. 2023), leading to DOM with lower molecular weight and higher aromaticity that promotes stronger interactions with contaminants (Hameed et al. 2023). Despite extensive research on biochar-metal interactions (Chen et al. 2019; Fan et al. 2020; Ke et al. 2023), the influence of biochar-derived DOM on adsorption efficiency and its complexation mechanisms with heavy metals remain underexplored. This knowledge gap impedes the optimization of biochar-based remediation technologies, especially under environmentally realistic conditions where DOM release is inevitable.

Advanced spectroscopic techniques, known for their sensitivity and non-destructive characteristics, have been extensively utilized to investigate DOM-metal interactions (Chen et al. 2015; Zhou et al. 2023). However, the complexity of DOM often results in overlapping peaks in three-dimensional excitation-emission matrix fluorescence spectra (3D-EEM), necessitating the use of parallel factor analysis (PARAFAC) for component separation; similarly, ultraviolet–visible (UV–vis) absorption spectra frequently exhibit obscured features, prompting the application of differential log-transformed absorption spectra to reveal additional binding sites and heterogeneity (Chen et al. 2015; Hou et al. 2023). Within PARAFAC components, fluorescence peaks may represent distinct substances with varying affinities for heavy metals, highlighting the importance of analyzing individual peaks to unravel the binding mechanisms (Zeng et al. 2017). The combination of hetero-2DCOS with EEM-PARAFAC and UV–vis differential log-transformed absorption spectra offers a powerful approach to decipher the reaction sequences between fluorescence groups and absorption bands. For instance, Cui et al. (2020) utilized 2DCOS coupled with EEM-PARAFAC and the modified Stern–Volmer equation to demonstrate that humic-like components in compost-derived DOM exhibit higher binding capacity and kinetics for Hg(II). Similarly, Liu et al. (2022) employed 2DCOS, hetero-2DCOS, and moving-window 2DCOS (MW2DCOS) alongside EEM-PARAFAC to delineate the binding sequences and sites of DOM from different river sections with Cu(II). Additionally, Habibul and Chen (2018) utilized 2DCOS, hetero-2DCOS, synchronous fluorescence spectra (SFS), and UV–vis spectroscopy to investigate the binding response sequence of fluorescence groups and absorption bands in humic-like substances for Pb(II). Their findings revealed that carboxyl groups react prior to phenolic groups, with these changes preceding fluorescence band shifts. Consequently, integrating 3D-EEM and UV–vis spectroscopy with two-dimensional correlation spectroscopy offers a promising approach to elucidate the sequential interactions between heavy metals and functional groups in DOM. Nevertheless, to date, only a limited number of studies have employed this combination of complementary techniques to explore the sequence, specificity, and heterogeneity of metal binding by biochar-derived DOM. Understanding these molecular-level interactions is essential for accurately predicting DOM behavior in complex environmental systems and for guiding the development of more effective biochar materials for heavy metal remediation.

The primary objective of this study is to elucidate the binding mechanisms between biochar-derived DOM and Pb(II) using a multi-spectroscopic approach and to evaluate the influence of DOM on the adsorption process. Specifically, the study aims to: (1) systematically assess the impact of DOM on biochar adsorption capacity through controlled experiments; (2) characterize the structural and functional changes in DOM-Pb(II) complexes using EEM and UV–vis spectroscopy; and (3) employ 2DCOS and hetero-2DCOS to investigate the response sequences of individual fluorescence peaks and absorption bands during DOM-Pb(II) interactions. The integration of hetero-2DCOS with EEM-PARAFAC and UV differential log-transformed absorption spectroscopy offers a novel analytical framework for simultaneous characterization of fluorescence and absorbance signatures in DOM-contaminant systems. This multidimensional approach enables comprehensive elucidation of Pb(II) binding mechanisms with DOM components, significantly enhancing the analytical precision required for developing targeted environmental remediation strategies.

2 Materials and methods

2.1 Preparation of biochar and extraction of DOM

Corn straw was obtained from Harbin City, Heilongjiang Province, China. The straw was washed with deionized water, dried, and ground into a fine powder, which was then sieved through a 100-mesh screen to prepare the raw material for biochar production. Based on its high DOM content and efficient adsorption capacity for inorganic pollutants, low-temperature biochar produced at 300 °C was selected for this study (Ahmad et al. 2014; He et al. 2021). The sieved corn straw powder was placed in a tube furnace (BTF 1200C, Anhui B E Q Equipment

Technology Co., Ltd.), and pyrolyzed at 300 °C. To ensure an anaerobic environment, nitrogen gas was introduced into the furnace at a flow rate of 0.4 L min^{-1} for 15 min prior to pyrolysis to remove residual oxygen. The pyrolysis was conducted under continuous nitrogen flow. After pyrolysis, the biochar was stored in a self-sealing bag. Water-washed biochar (WBC) was prepared following the method described by Lou et al. (2016). Briefly, Milli-Q ultrapure water was added to the biochar, and the mixture was heated in a water bath at 100 °C for 3 h. The mixture was then agitated on a rotary shaker at 220 rpm for 24 h at room temperature (25 °C). The solution was filtered through a 0.45 μm membrane, rinsed multiple times with Milli-Q ultrapure water, and the remaining biochar on the filter membrane was collected, dried, and stored in sealed containers.

DOM was extracted by adding biochar to an appropriate volume of Milli-Q ultrapure water in a plastic bottle, followed by shaking at 25 °C in the dark for 24 h. The resulting solution was filtered through a 0.45 μm membrane to obtain DOM, which was stored in the dark at 4 °C. The dissolved organic carbon (DOC) concentration was measured using a total organic carbon (TOC) analyzer (Vario TOC, Elementar, Germany). DOM samples were collected at various time intervals (0.5, 1, 3, 8, 16, and 24 h), and their DOC concentrations and 3D-EEM fluorescence spectra were analyzed.

2.2 Adsorption experiment

To investigate the potential influence of DOM on the adsorption of Pb(II) by biochar, the adsorption performance of untreated biochar (BC) and WBC was compared. In the kinetic adsorption experiment, biochar was mixed with a Pb(II) solution (initial concentration: 100 mg L^{-1}) at a ratio of 1 g L^{-1}. The mixture was agitated in a constant-temperature shaker at 220 rpm and 25 °C. Samples were collected at intervals of 5, 10, 30, 60, 120, 240, 480, 720, and 1440 min, filtered through a 0.45 μm membrane, and the Pb(II) concentration in the filtrate was determined using an atomic absorption spectrometer (Thermo, ICE^{TM}3500). The removal efficiency and adsorption capacity of biochar for Pb(II) were calculated. In the isothermal adsorption experiment, Pb(II) concentrations ranged from 0 to 500 mg L^{-1}, and the procedures were identical to those in the kinetic adsorption experiment. In the isothermal adsorption experiments, initial Pb(II) concentrations were set at 50, 100, 150, 200, 250, and 500 mg L^{-1} to cover a wide concentration range. The biochar dosage (1 g L^{-1}), temperature (25 °C), and shaking speed (220 rpm) were kept constant, aligning with the conditions employed in the kinetic adsorption experiments. Following 24 h of equilibration, the suspensions were filtered through 0.45 μm membranes, and the residual Pb(II) concentrations in the filtrates were quantified. The resulting adsorption data were subsequently fitted to appropriate isotherm models to evaluate the adsorption capacity and elucidate the underlying mechanisms. All experiments were conducted in triplicate to ensure reproducibility and reliability of the results.

2.3 Quenching titration experiment

Quenching titration experiments were conducted to evaluate the complexation of DOM with Pb(II) and to elucidate the underlying mechanisms. To minimize the inner filter effect (IFE), the DOC concentration was adjusted to 10 mg L^{-1}, and IFE corrections were applied using an Aqualog fluorescence spectrometer (Horiba, Japan). A 0.1 mol L^{-1} $Pb(NO_3)_2$ solution was incrementally added to a 50 mL DOM solution in a conical flask, generating a series of Pb(II) concentrations ranging from 0 to 200 μmol L^{-1}.

The pH of the mixed solution was adjusted to 7 ± 0.05 using 0.1 mol L^{-1} HCl and 0.1 mol L^{-1} NaOH, ensuring that the total volume of acid, base, and $Pb(NO_3)_2$ solution added did not exceed 500 μL (less than 1% of the total solution volume) to minimize dilution effects. The solution was shaken in the dark at 25 °C for 24 h to ensure complete complexation. Subsequently, the solution was analyzed using 3D-EEM fluorescence spectroscopy, and UV–vis absorbance spectra were measured concurrently.

2.4 UV–Vis and 3D-EEM

UV–vis and 3D-EEM measurements were conducted simultaneously using an Aqualog fluorescence spectrometer (Horiba, Japan). Absorbance spectra were recorded over a wavelength range of 200–600 nm using a 1 cm quartz cuvette. The integration time was set to 0.2 s with a step size of 5 nm, and a 150 W argon arc lamp served as the excitation light source.

Due to the inherent complexity of the original UV–vis absorbance spectra, differential methods, including differential and log-transformed absorbance spectra, were employed to enhance data interpretability. The corresponding formulas are as follows:

$$DA_\lambda = A_{\lambda,i} - A_{\lambda,ref} \quad (1)$$

$$DLnA_\lambda = LnA_{\lambda,i} - LnA_{\lambda,ref} \quad (2)$$

where DA_λ and $DlnA_\lambda$ represent the differential spectra of the original and log-transformed absorbance, respectively; $A_{\lambda,i}$ and $A_{\lambda,ref}$ denote the absorbance intensities at specific Pb(II) concentrations and the reference absorbance intensity (i.e., in the absence of Pb(II)), respectively.

2.5 Complexation model and PARAFAC analysis

The Stern–Volmer equation was employed to investigate the static quenching mechanism of fluorophores, assuming a 1:1 stoichiometric ratio for metal-complex associations. However, when fluorescence quenching data at specific wavelengths indicate the existence of multiple binding sites, this assumption may no longer hold. To address this limitation, the modified Stern–Volmer equation was applied, which accounts for the contribution of unquenched fluorescence (Cui et al. 2020; Liu et al. 2022).

In this study, the modified Stern–Volmer equation was used to determine the binding parameters of DOM-Pb(II) complexes, as expressed below:

$$\frac{F_0}{F_0-F}=\frac{1}{fKC_{Pb(\Pi)}}+\frac{1}{f} \quad (3)$$

where F_0 and F denote the fluorescence intensities of the DOM sample in the absence and presence of Pb(II), respectively, as measured by 3D-EEM fluorescence spectroscopy; K represents the fluorescence quenching constant, reflecting the stability of the DOM- Pb(II) complex, while f signifies the fraction of DOM components that bind to Pb(II). The parameters f and K were derived by plotting $F_0/(F_0\text{-}F)$ against $1/C_{Pb(II)}$ and performing linear regression analysis.

PARAFAC analysis was conducted using the EEMstoolkit package (Shu et al. 2024). The analytical procedure involved scanning the EEM of Milli-Q ultrapure water as a blank reference prior to PARAFAC modeling. All sample EEMs were Raman-normalized (R.U.) using the blank data at Ex = 350 nm (Lawaetz and Stedmon 2009), followed by correction for Rayleigh and Raman scatterings effects. The analysis encompassed DOM samples with Pb(II) concentrations ranging from 0 to 200 μmol·L^{-1}, with a minimum of 20 EEM spectra collected per concentration to ensure model stability. Model selection was performed through residual analysis, core consistency diagnostic, and split-half validation (provided in the Supporting Information, SI, Fig. S1), resulting in the identification of a three-component model. The spectral characteristics, including Fmax values, Ex loadings, and Em loadings, were quantified for each PARAFAC component. To validate the reproducibility of the identified components, the results were cross-referenced with the OpenFluor online database (http://www.openfluor.org) (Murphy et al. 2014), with the component similarity confirmed through Tucker congruence coefficient (TCC) exceeding 0.9.

2.6 2DCOS analysis

To investigate the sequential variations in the absorption bands and fluorescence groups of DOM, 2DCOS and hetero-2DCOS analyses were employed. These analyses were performed using differential log-transformed absorption spectra and the Ex loadings of PARAFAC components, with Pb(II) concentration as the perturbation factor. The 2DCOS calculations were conducted following established methodologies by Noda and Ozaki (Noda and Ozaki 2005; Noda 2016), and the "2DShige" software (Kwansei Gakuin University, Japan) was utilized to generate the corresponding synchronous and asynchronous correlation maps and matrices. Data processing and visualization were carried out using Origin 2020 software. For a detailed explanation of 2DCOS analysis, readers are directed to prior studies (Hur and Lee 2011; Chen et al. 2015; Huang et al. 2018).

3 Results and discussion

3.1 SEM and DOC analysis

Scanning electron microscopy (SEM) was utilized to characterize the surface morphology of biochar (**Text S1**). As illustrated in Fig. 1(a), the biochar samples display a highly porous structure, with pore sizes ranging from approximately 30 to 40 μm, which may contribute to the biochar's enhanced pollutant removal capacity. Figure 1(a) and (c) reveal that the biochar surfaces are densely covered with particulate matter, consistent with the presence of DOM on the biochar (Wang et al. 2023). In contrast, the WBC, depicted in Fig. 1(b) and (d), maintains a porous structure but exhibits more fragmentation, likely due to the washing process. Additionally, the reduced presence of particles on the WBC surface provides additional evidence that DOM primarily exists as surface-attached particles on the biochar.

To further verify that the detachment of these particles is associated with DOM, batch sampling of the BC solution was conducted at intervals ranging from 0 to 24 h. A control group was maintained without agitation for 24 h. DOM was subsequently extracted for DOC and EEM-PARAFAC analysis (detailed EEM-PARAFAC results are discussed in the following section). As illustrated in Fig. S2, the DOC concentration increased steadily over the shaking period, reaching 18.88 mg L^{-1} and after 24 h, compared to 14.79 mg L^{-1} in the control group. This progressive increase in DOC concentration confirms that the particles detaching from the biochar surface are indeed DOM. This is particularly significant, as DOM has been demonstrated to play a pivotal role in the environmental behavior of heavy metals. DOM, which is abundant in biochar, can form strong complexes with various metal ions, potentially enhancing their mobility or modifying their bioavailability and retention in soils (Zhang et al. 2020). Notably, biochar produced under low-temperature pyrolysis conditions retains higher levels of DOM (Guo et al. 2022), which may further intensify its interaction with metal ions through complexation

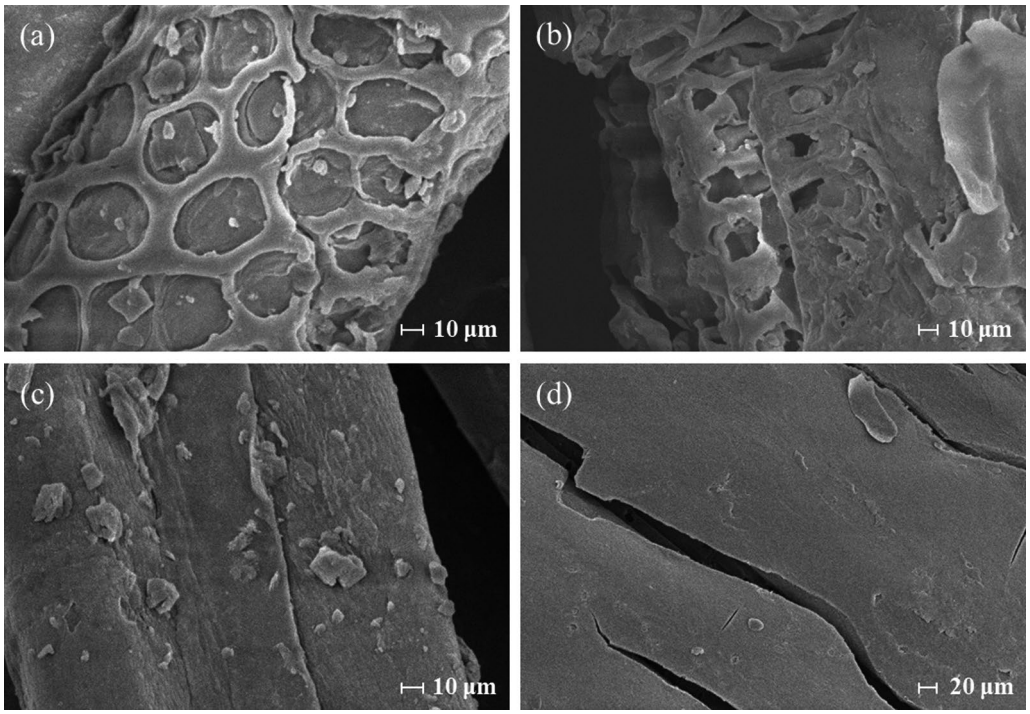

Fig. 1 SEM images of biochar: BC: (**a**), (**c**); WBC: (**b**), (**d**)

mechanisms. Consequently, to comprehensively evaluate the long-term remediation performance of biochar and precisely predict the environmental fate of heavy metals in biochar-amended systems, it is crucial to first elucidate the underlying interaction mechanisms between biochar-derived DOM and heavy metal ions such as Pb(II).

3.2 Kinetic and isothermal adsorption analysis

Kinetic adsorption experiments were conducted for both BC and WBC, and the data were fitted using pseudo-first-order and pseudo-second-order models (Text S2). The fitted curves and corresponding parameters are presented in Fig. S3a and Table S1. Based on the regression coefficients, the pseudo-second-order model ($R^2 = 0.997$ for BC and $R^2 = 0.999$ for WBC) provided a better fit for the kinetic adsorption of Pb(II) compared to the pseudo-first-order model ($R^2 = 0.952$ for BC and $R^2 = 0.006$ for WBC). These results suggest that the adsorption of Pb(II) by both BC and WBC is chemically driven, and the removal of DOM does not alter the fundamental adsorption mechanism of BC. The adsorption capacity derived from the pseudo-second-order model fitting was 96.2 mg g^{-1} for BC (Table S1), which is significantly higher than those reported for many other plant-derived biochars under similar conditions. For example, biochar produced from rice straw (pyrolyzed at 300 °C, 54.79 mg g^{-1} (Wang et al. 2024)) and corn straw (pyrolyzed at 500 °C, 21.3 mg g^{-1} (Yang et al. 2023)) exhibited lower adsorption capacities, emphasizing the outstanding performance of the biochar prepared from corn straw at a relatively low pyrolysis temperature in this study. In contrast, the adsorption capacity of WBC was only 35.0 mg g^{-1}, highlighting the critical role of DOM in enhancing the adsorption capacity of biochar. This indicates that DOM may promote the exposure or retention of functional groups and active sites conducive to Pb(II) binding, thus improving adsorption efficiency.

For the isothermal adsorption analysis, the Langmuir, Freundlich, and Temkin models were applied to describe the adsorption behavior of BC and WBC (Text S3), as illustrated in Fig. S3b. According to the regression coefficients presented in Table S2, the Freundlich model ($R^2 = 0.961$ for BC and $R^2 = 0.876$ for WBC) provided a better fit to the adsorption data than the Langmuir model ($R^2 = 0.887$ for BC and $R^2 = 0.770$ for WBC). This suggests that the adsorption processes on both BC and WBC are more consistent with heterogeneous multilayer adsorption (Sebastian et al. 2019; Fan et al. 2022). The Freundlich parameter n reflects the adsorption affinity of biochar for Pb(II). When $n > 1$, the adsorption conditions are favorable, with higher n values indicating stronger adsorption affinity (Fan et al. 2017; Tian et al. 2025). In this study, both BC ($n = 6.62$) and WBC ($n = 2.32$) exhibited favorable adsorption of Pb(II), with

BC demonstrating a significantly higher n value, suggesting a stronger adsorption affinity for Pb(II). Additionally, the Temkin isotherm model, which assumes a linear decrease in adsorption energy with increasing surface coverage, is particularly suitable for describing chemical adsorption processes (Cui et al. 2024). The R^2 values for BC (0.945) and WBC (0.812) further support that the adsorption process aligns well with the characteristics of chemical adsorption.

3.3 FTIR and XPS analysis

The FTIR spectra of BC, WBC, and DOM before and after Pb(II) adsorption/ titration are presented in Fig. 2. The results reveal the presence of various functional groups at a pyrolysis temperature of 300 °C. A broad absorption band at 3419 cm^{-1} corresponds to O–H stretching vibrations (Chen et al. 2023), while the peaks at 2920 cm^{-1} and 2848 cm^{-1} are attributed to the stretching vibrations of aliphatic $–CH_2$ and $–CH_3$ groups (Chen et al. 2020). In BC (Fig. 2a), the C=O stretching vibration shifted slightly from 1605 to 1607 cm^{-1} after Pb(II) adsorption, and the C–O stretching vibration shifted from 1104 to 1105 cm^{-1}, indicating the involvement of oxygen-containing functional groups in Pb(II) complexation (Wan et al. 2021; Yue et al. 2025). In contrast, the C=C peak at 1440 cm^{-1} remained unchanged, suggesting that aromatic groups played a minimal role in Pb(II) binding. For WBC (Fig. 2b), no significant shifts were observed in the C=C, C–O, and C=O peaks after Pb(II) adsorption. However, the ether C–O stretching peak shifted from 1381 to 1385 cm^{-1} with increased intensity, indicating partial participation of these groups in Pb(II) binding. This finding aligns with the lower adsorption capacity of WBC (Li et al. 2024a). In the DOM samples (Fig. 2c), several key spectral shifts were observed after Pb(II) titration: the C=O stretching peak shifted from 1585 to 1598 cm^{-1}, C=C shifted from 1412/1385 to 1385/1359 cm^{-1}, and C–O shifted from 1102 to 1095 cm^{-1} (Yue et al. 2025). These observations suggest

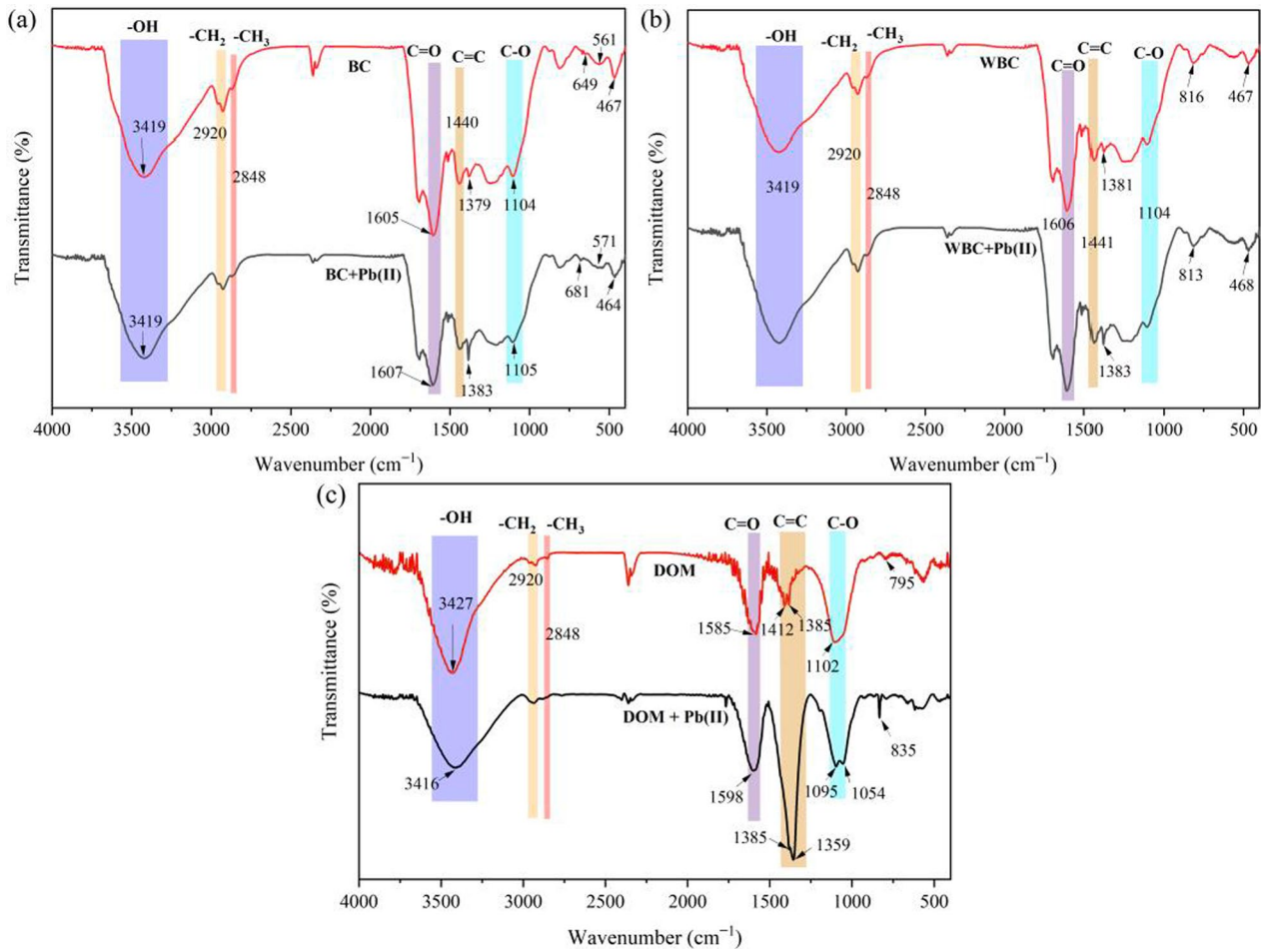

Fig. 2 FTIR spectra of BC (**a**), WBC (**b**), and DOM (**c**) before and after Pb(II) binding

that DOM retains abundant active groups capable of participating in Pb(II) complexation.

XPS further confirmed the critical role of oxygen-containing functional groups in Pb(II) binding (**Text S1**). As depicted in Fig. 3a, the C 1 s spectra of BC and its derived DOM consist of three primary components: C–C, C–O, and C=O (Li et al. 2024b). In comparison to BC, WBC demonstrated a diminished proportion of C–O (Fig. 3b), presumably attributed to the removal of surface-bound organics during water washing. Following Pb(II) adsorption (Fig. 3c), the proportions of C–O and C=O in BC decreased by 12.77% and 8.04%, respectively, indicating their active participation in the adsorption process. Moreover, both peaks exhibited increased binding energies, which suggests a reduction in electron density due to Pb(II) interaction. In contrast, for WBC (Fig. 3d), the C=O content decreased marginally (by 3.25%), while C–O increased by 16.14%, reflecting the involvement of these functional groups and the reduced Pb(II) binding capacity of WBC. The DOM spectra (Fig. 3e) displayed analogous trends, with a 15.63% decrease in oxygenated groups after Pb(II) titration (Fig. 3f), along with shifts in binding energies for all components. These observations substantiate the active engagement of oxygen-containing groups in Pb(II) coordination. Additionally, the O 1 s spectra (Fig. S4a–f), encompassing peaks corresponding to C=O (carbonyl or quinone), C–OH (hydroxyl), and O=C-O (carboxyl), revealed shifts in binding energies post Pb(II) adsorption, corroborating the involvement of these functional groups in metal binding (Chen et al. 2021). The Pb 4f spectra (Fig. 3g–i) confirmed the presence of Pb(II) on the biochar surfaces and within the DOM complexes. The predominant species identified was $Pb_3(OH)_2(CO_3)_2$ (83.41%), with a minor contribution

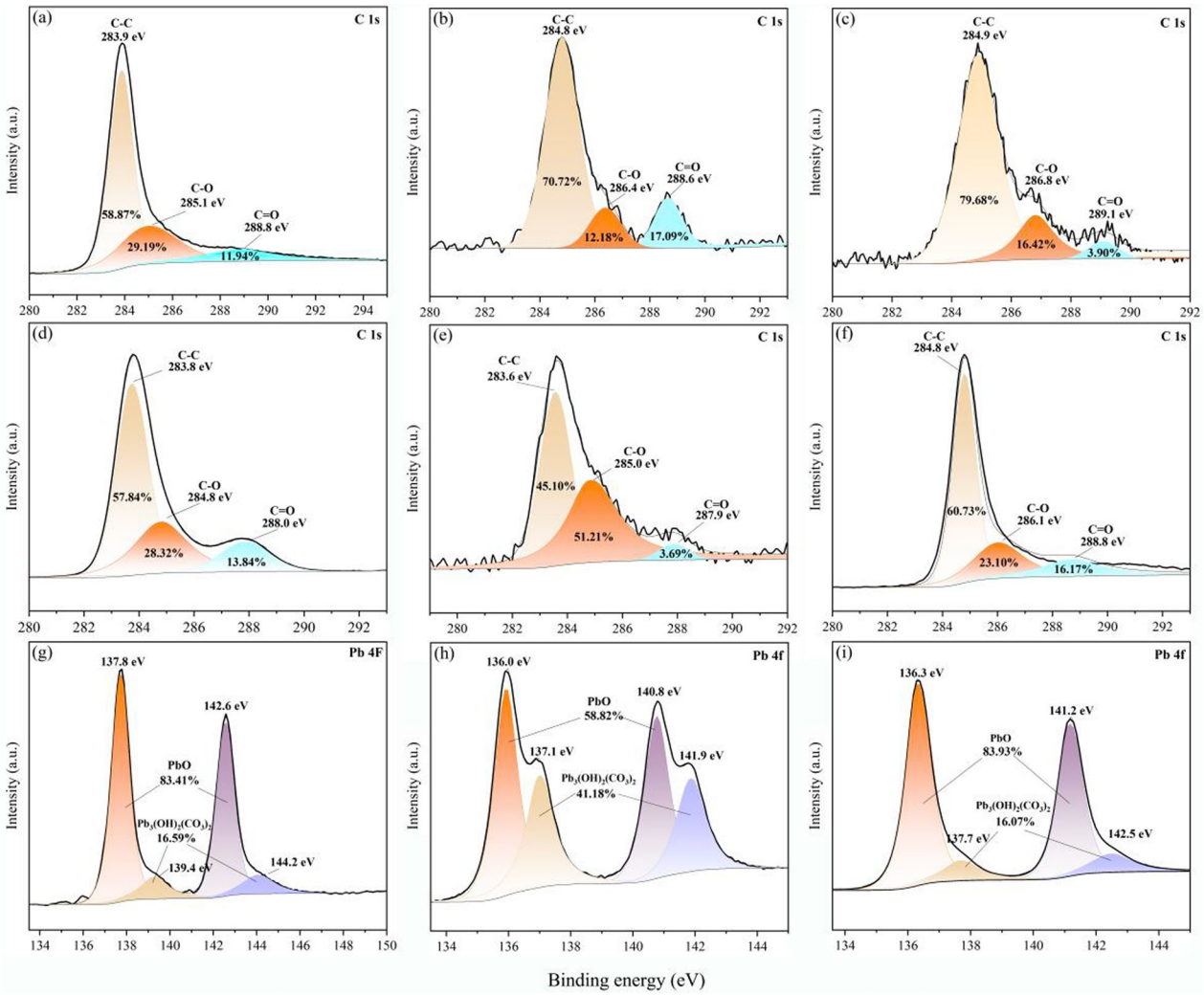

Fig. 3 XPS C 1s and Pb 4f spectra of BC, WBC, and DOM before and after Pb(II) binding: (**a**, **b**) C 1s spectra of BC and WBC; (**c**, **g**) C 1s and Pb 4f spectra of BC–Pb(II); (**d**, **h**) C 1s and Pb 4f spectra of WBC–Pb(II); (**e**) C 1s spectrum of DOM; (**f**, **i**) C 1s and Pb 4f spectra of DOM–Pb(II)

from PbO (16.59%). This distribution pattern remained consistent across all samples (BC, WBC, and DOM). Collectively, these findings indicate that oxygen-containing functional groups on biochar surfaces and within DOM are crucial for Pb(II) retention, with complexation serving as the primary mechanism and co-precipitation acting as a secondary process (Wang et al. 2021).

3.4 UV–vis differential absorption spectra and log-transformed spectral analysis

The initial UV–vis absorption spectra of DOM typically exhibit an exponential decrease in absorbance with increasing wavelength, with overall spectral characteristics being less pronounced (Chen et al. 2002). In this study, the original spectra displayed a similar exponential decay trend (Fig. 4a), accompanied by a shoulder peak at approximately 275 nm. This peak is indicative of the π-π electronic transition in the ultraviolet region, characteristic of phenolic compounds (Janot et al. 2010). Furthermore, an increase in DOM absorbance at shorter wavelengths was observed with increasing Pb(II) concentration. This phenomenon is likely due to the presence of functional groups in DOM, such as -COOH, -OH, and aromatic structures, which possess lone electron pairs capable of forming complexes with metal ions, thereby enhancing electron delocalization and increasing absorbance (Bai et al. 2008). The differential absorption spectrum (Fig. 4b) revealed a distinct peak around 208 nm, which intensified with higher metal concentration. A slight redshift in the peak position was also noted, suggesting interactions between DOM and metal ions that may alter the microenvironment of DOM chromophores.

Given the quasi-exponential nature of the absorption spectra, log-transformation of the original data was employed to better highlight wavelength or peak sensitivities relevant to DOM-metal interactions. As shown in Fig. 4(c), the log-transformed spectra exhibited a nearly linear decrease with increasing wavelength, with distinct

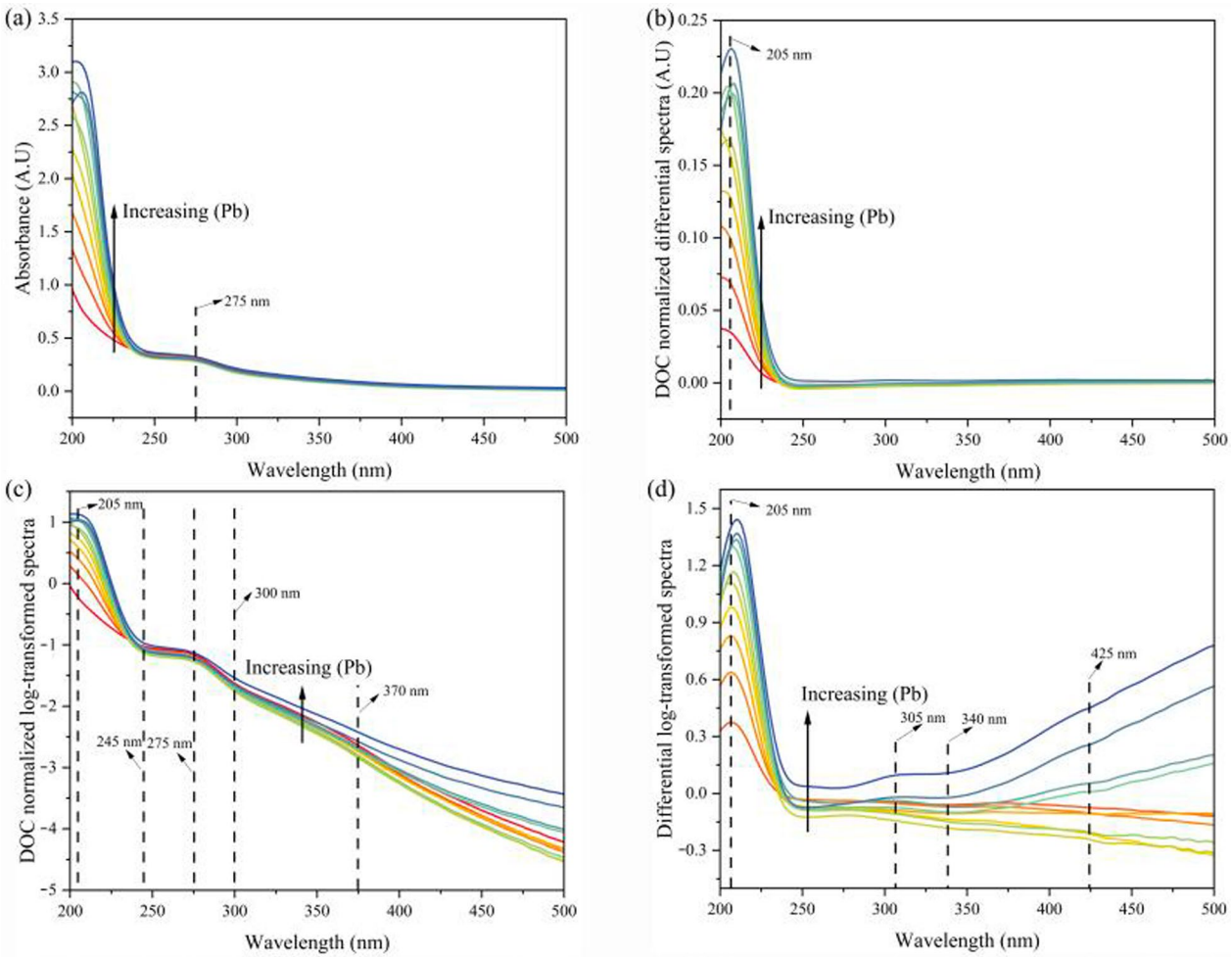

Fig. 4 Effects of increasing Pb(II) concentration on (**a**) original absorption spectra of DOM samples, (**b**) DOC-normalized differential absorption spectra, (**c**) log-transformed absorption spectra, and (**d**) differential log-transformed absorption spectra

segments of varying slopes identified (e.g., 205–245 nm, 245–275 nm, 275–300 nm, and > 370 nm). This segmentation underscores the heterogeneity of active sites and functional groups involved in DOM-Pb(II) binding, demonstrating the utility of log-transformation in elucidating the specificity of DOM-metal interactions.

To further explore the binding sites, differential log-transformed absorption spectra were analyzed. These spectra have been shown to provide additional insights into chromophore interactions within DOM, even for those with weak interaction strengths, and are particularly sensitive to processes such as DOM deprotonation and metal complexation (Yan et al. 2013; Lu et al. 2017). As depicted in Fig. 4(d), the differential log-transformed absorption spectra revealed multiple characteristic peaks or bands, with intensities increasing upon Pb(II) addition across various wavelength regions (205 nm, 305 nm, 340–425 nm, and > 425 nm). Notably, the intensity increase was more pronounced at shorter wavelengths (e.g., 205 nm) compared to longer wavelengths, indicating that chromophores at shorter wavelengths play a more significant role in Pb(II) complexation. These findings highlight the utility of differential log-transformed absorption spectra in revealing the heterogeneity of DOM chromophores' binding properties, including site distribution, sensitivity, and complexation degree.

3.5 EEM-PARAFAC analysis

In the initial EEM spectra, a pronounced humic-like peak was observed within the Ex/Em range of 230–260 nm/355–450 nm (Fig. S5). This peak exhibited a significant reduction in fluorescence intensity with increasing Pb(II) concentration. However, due to the potential overlap of peaks in the original EEM spectra, which could obscure the spectral analysis of DOM, PARAFAC decomposition was employed to resolve fluorescence signals into distinct components, thereby mitigating the impact of peak overlap. This approach enabled a more detailed investigation of the binding interactions between fluorescence components and Pb(II) (Li et al. 2017; Zhang et al. 2021).

The EEM-PARAFAC analysis identified three distinct components (Fig. 5), with peak positions corresponding to C1 (Ex/Em = 230/385 nm), C2 (Ex/Em = 240, 340/445 nm), and C3 (Ex/Em = 230, 270, 400/303, 492 nm). Specifically, component C1 exhibited characteristics similar to the humic-like A peak and was classified as UV humic-like (Sondergaard et al. 2003; Gao and Guéguen 2018). Component C2 combined features of the traditional UV humic-like A peak and the visible humic-like C peak, indicative of terrestrial humic-like substances with higher relative aromaticity and molecular weight (Chen et al. 2018). Component C3 was more unique, characterized by multiple Em wavelengths. Its peaks were primarily distributed at two distinct Em values: 303 nm and 492 nm. According to the OpenFluor database matching, the long-wavelength (Em = 492 nm) peak was specifically identified as large humic-like substances derived from cultivated soil (Romero et al. 2019). The limited detection of short-wavelength signals (Em = 303 nm), likely due to their relatively low fluorescence intensity, showed spectral similarity to the traditional tyrosine-like B peak. These observations suggest that component C3 represents a combination of humic-like and tyrosine-like substances. To ascertain whether the tyrosine-like fluorescence observed in component C3 originated from the raw biomass or was generated during the pyrolysis process, EEM-PARAFAC analysis was performed on DOM extracted from untreated corn straw. The analysis identified a component with spectral characteristics closely resembling those of C3, exhibiting both humic-like and tyrosine-like features (Fig. S6). These findings indicate that the tyrosine-like signals in C3 were predominantly inherited from the original lignocellulosic feedstock rather than being newly formed during the pyrolysis process.

In the validation experiment, the fluorescence intensities of the three DOM components increased progressively with shaking time (Fig. S7). Specifically, the fluorescence intensity (R.U.) of the control group (C1 = 0.082, C2 = 0.039, C3 = 0.039) was significantly lower than that of the experimental group (C1 = 0.122, C2 = 0.060, C3 = 0.063). These observations align with the findings from DOC analysis, and the SEM results further corroborated that DOM consists of particulate matter adsorbed onto BC, which can readily detach from the biochar surface and dissolve into water.

As shown in Fig. S8, the fluorescence quenching titration experiment demonstrated that all three components underwent a quenching effect, with their maximum fluorescence intensities (Fmax) decreasing as Pb(II) concentration increased, indicating complexation with Pb(II). In this study, we investigated the interactions between the PARAFAC components and Pb(II), and calculated the binding parameters of humic-like substances with Pb(II) in DOM using the modified Stern–Volmer equation. The corresponding spectra are presented in Fig. S9 and Table S3. The log K_M values for C1, C2, and C3 were 4.085, 3.693, and 4.160, respectively, revealing that the C3 component in DOM exhibits the strongest binding affinity with Pb(II), followed by UV humic-like (C1) and visible humic-like substances (C2). This finding is consistent with previous studies, where most log K_M values typically fall within the range of 3–5 (Xing et al. 2020). Besides, it is noteworthy that a single DOM PARAFAC component often comprises multiple fluorescence peaks, making it

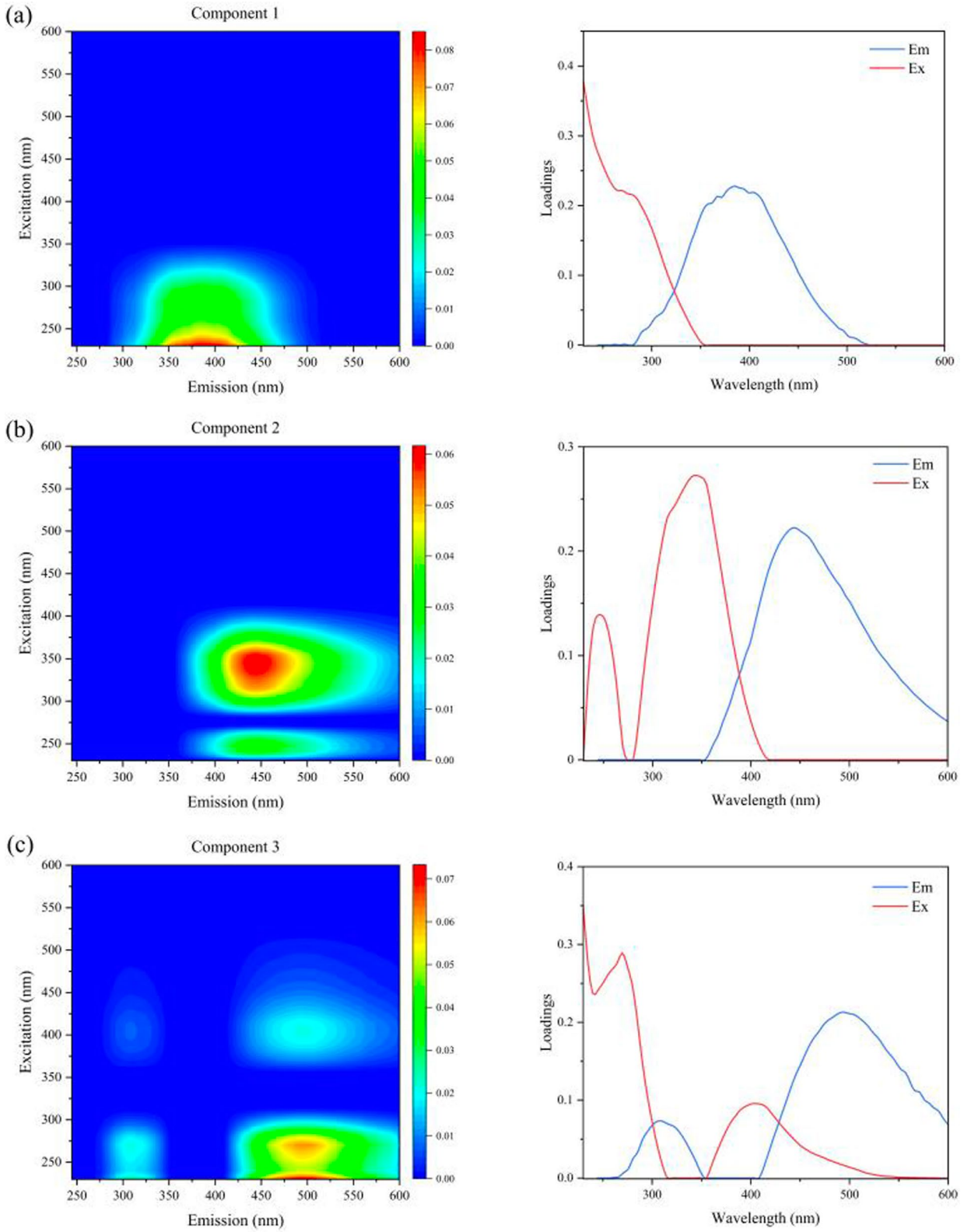

Fig. 5 DOM fluorescence spectra obtained by the EEM-PARAFAC method: (**a**) C1, (**b**) C2, (**c**) C3

challenging to ascertain whether all fluorescence peaks within the same component participate in Pb(II) complexation, as well as their respective contributions and reaction rates. Therefore, further research is necessary to elucidate the detailed interactions between Pb(II) and DOM.

3.6 2DCOS and hetero-2DCOS combined with EEM spectral analysis

2DCOS and hetero-2DCOS can be utilized to investigate the sensitivity of fluorescence peaks in the DOM PARAFAC components to Pb(II) complexation (Text S4). As previously demonstrated, each DOM PARAFAC component likely contains multiple fluorescence peaks at the same Em, with their corresponding Ex values providing insights into distinct fluorescence peaks. By utilizing 2DCOS, the relationship between Pb(II) complexation kinetics and DOM fluorescence peaks can be elucidated through the analysis of Ex values. Additionally, since only one fluorescence peak is observed in component C1, the investigation of peak shift order primarily focuses on components C2 and C3.

In the synchronous map of Pb(II) binding with C2 (Fig. 6a), the correlation peaks at 240 nm (C21) and 340 nm (C22) exhibit negative values. Table S4 summarizes the signs of each cross-peak in the 2DCOS maps. According to the peak identification and interpretation rules for the 2DCOS maps (Noda and Ozaki 2005; Noda 2016), positive values in the synchronous map indicate a homologous relationship, whereas negative values suggest that the peaks change in opposite directions under Pb(II) perturbation. This indicates that C21 and C22 undergo changes in opposite directions. In contrast, the asynchronous map (Fig. 6b) shows a positive correlation between C21 and C22. By integrating the signs from both the synchronous and asynchronous maps, the sequence of fluorescence peak changes can be determined. Based on Noda's rule (Noda and Ozaki 2005; Noda 2016), the order of Pb(II) binding in C2 is as follows: C22 → C21. For C3, in the synchronous map (Fig. 6c), the correlation peak between C31 at 230 nm and C32 at 270 nm is negative, while the correlation peak between C31 at 230 nm and C33 at 400 nm is positive. Additionally, the correlation peak between C32 at 270 nm and C33 at 400 nm is negative. These observations indicate that the change in C32 differs from those in C31 and C33. In the asynchronous map (Fig. 6d), the cross-peaks between C31 and C32, and C31 and C33 are negative, while the cross-peak between C32 and C33 is positive. According to Noda's rule (Noda and Ozaki 2005; Noda 2016), the order of Pb(II) binding in C3 is as follows: C33 → C31 → C32.

It is noteworthy that, compared to C1 and C2, the fluorescence peaks of C3 exhibit two distinct Em under the same Ex. To differentiate these peaks, they are provisionally designated as C3-1 and C3-2. Subsequently, the fluorescence peaks are further categorized into C3-11, C3-12, C3-13 for C3-1, and C3-21, C3-22, C3-23 for C3-2. As illustrated in Fig. S10, an analysis of the fluorescence intensity changes for each peak in C3 reveals that the most significant fluorescence quenching effects occur in C3-21 and C3-23. Consequently, 2DCOS synchronous and asynchronous maps were generated for the fluorescence at the Em values corresponding to C3-2, as depicted in Fig. S11. These findings align with the 2DCOS analysis based on the Ex loadings of C3 (Fig. 6c and d), thereby validating the appropriateness of using the Ex loadings of C3 to characterize the variations in the fluorescence peaks of C3.

Additionally, it is important to highlight that both C3-13 (exhibiting notably low fluorescence intensity) and C3-22 demonstrate minimal intensity variation (Fig. S10), collectively suggesting their limited contribution to Pb(II) complexation. In contrast, the fluorescence intensity of C21 progressively increases with rising Pb(II) concentration. A significantly negative correlation coefficient between C21 and C22 ($R = -0.929$, $p < 0.001$) was calculated, indicating an inverse relationship. Combined with the 2DCOS results for C2, this suggests that C21 likely arises from partial complexation between C22 and Pb(II). Similarly, the fluorescence intensities of C3-11 and C3-12 gradually increase with Pb(II) concentration, potentially due to Pb(II)-induced alterations in the molecular environment of protein-like components or the combined effects of multiple interaction mechanisms. This increase in fluorescence intensity can be attributed to two primary factors: (1) Pb(II) may induce structural changes in protein molecules, affecting their fluorescence quantum yield; and (2) the initial quenching of protein-like fluorescence by inorganic or organic substances may be reversed as Pb(II) displaces the original quenchers, forming more stable DOM-Pb(II) complexes and releasing protein-like components, thereby enhancing fluorescence intensity. Thus, the observed increase in protein-like fluorescence intensity likely results from changes in the molecular environment of protein-like components. Further research is required to elucidate these mechanisms and evaluate their environmental implications (Yamashita and Jaffé 2008).

To further investigate the binding capabilities of Pb(II) with fluorescence peaks across different PARAFAC components, hetero-2DCOS analysis was conducted based on Noda's rules (Noda and Ozaki 2005; Noda 2016). As illustrated in Fig. 7 and Table S4, for components C1 and C2, the synchronous map (Fig. 7a) reveals a negative correlation between C1 and C21 and a positive correlation between C1 and C22, confirming that changes

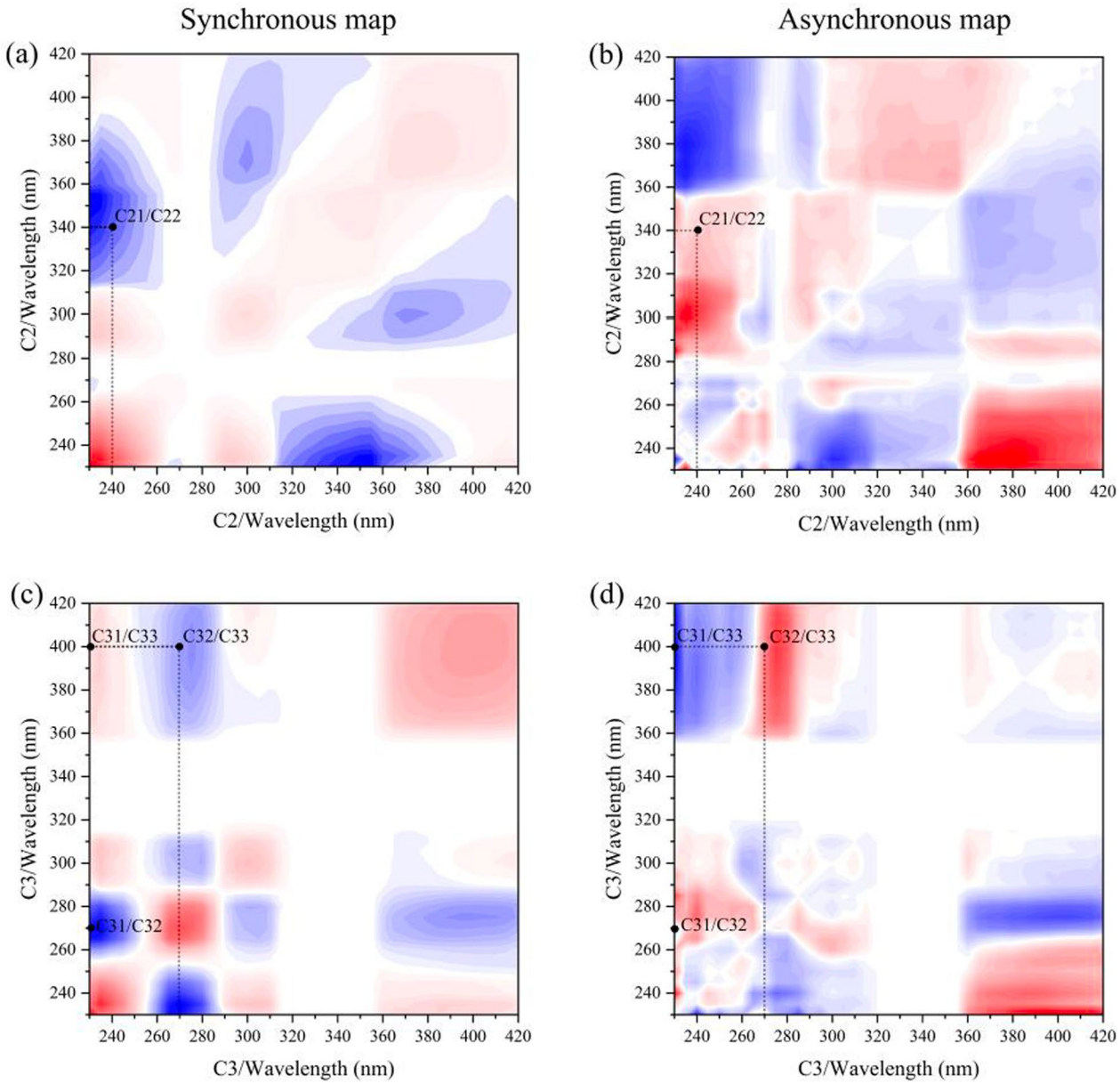

Fig. 6 Synchronous and asynchronous maps obtained via 2DCOS of PARAFAC components under Pb(II) concentration perturbation. (Red represents positive correlation, blue represents negative correlation)

in C21 and C22 occur in opposite directions. The asynchronous map (Fig. 7b) similarly shows a negative correlation between C1 and C21 and a positive correlation between C1 and C22. Based on these findings, the binding sequence of Pb(II) with the fluorescence peaks in C1 and C2 is: C1 → C22 → C21. In the synchronous and asynchronous maps of C1 and C3 (Fig. 7c and d), C1 displays positive correlations with both C31 and C33 and a negative correlation with C32. Consequently, the binding sequence in C1 and C3 is: C1 → C33 → C31 → C32. In the synchronous map of C22 and C3 (Fig. 7e), the correlation peak between C22 and C31 is negative, while the correlation peak with C32 and C33 is positive. In the asynchronous map (Fig. 7f), the cross-peak between C22 and C31 is negative, and the cross-peak with C32 and C33 is positive. Therefore, the reaction sequence is: C33 → C31 → C32 → C22. In summary, the binding sensitivity of Pb(II) to the fluorescence peaks in the three DOM components follows the order: C1 → C33 → C31 → C32 → C22 → C21. This suggests that the UV humic-like

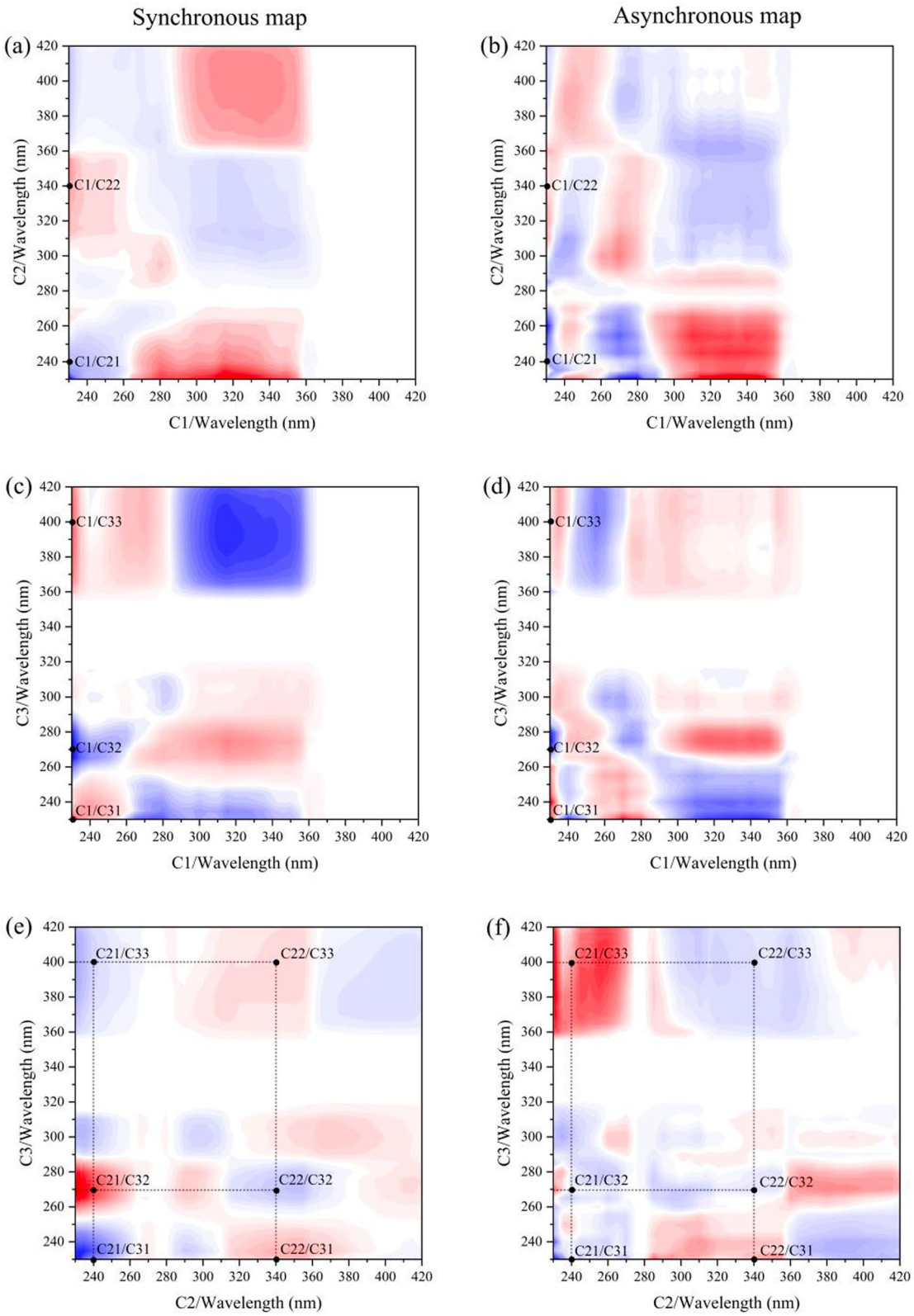

Fig. 7 Synchronous and asynchronous maps obtained via hetero-2DCOS of different PARAFAC components under Pb(II) concentration perturbation. (Red represents positive correlation, blue represents negative correlation)

substance at shorter wavelengths (C1) exhibits preferential reactivity, while the visible humic-like substances (C22) and the UV humic-like substance (C21) show the lowest sensitivity to Pb(II) complexation.

The 2DCOS synchronous and asynchronous maps derived from the UV differential log-transformed absorption spectra are presented in Fig. S12. In the synchronous map, a pronounced auto peak is observed at 205 nm, with a less intense auto peak at 305 nm; both peaks exhibit positive cross-correlation. The asynchronous map reveals a positive cross peak at the coordinates (205 nm, 305 nm), indicating that the absorbance change at 205 nm precedes that at 305 nm. Previous studies have suggested that the spectral region below 260 nm is associated with phenolic and carboxyl groups in DOM (Dryer et al. 2008; Lu et al. 2017; Xu et al. 2018). According to Noda's rule (Noda and Ozaki 2005; Noda 2016), conjugated carboxyl groups undergo alterations before phenolic groups, which is consistent with the observations made by Habibul and Chen (2018).

3.7 Hetero-2DCOS combined with UV-EEM spectral analysis

Hetero-2DCOS provides a comprehensive approach to elucidating the interactions between two distinct spectral probes during the complexation of Pb(II) with DOM. As illustrated in Fig. 8, by integrating hetero-2DCOS with Ex values derived from 3D-EEM fluorescence spectra and differential log-transformed absorption spectra, synchronous and asynchronous maps were generated. In these maps, the Ex values of each PARAFAC component are plotted on the x-axis, while the absorbance values are plotted on the y-axis. Analysis of the synchronous and asynchronous maps, as summarized in Table S5, further indicates that the cross-peaks between each fluorescence peak and the ultraviolet characteristic absorption peak at 205 nm exhibit opposite signs, whereas those with the ultraviolet characteristic absorption peak at 305 nm show the same sign. According to Noda's rule (Noda and Ozaki 2005; Noda 2016), the absorbance change at 205 nm precedes the changes in fluorescence peaks, which are then followed by the absorbance change at 305 nm. This sequence suggests that, during the complexation process, reactions involving conjugated carboxyl groups occur most rapidly, followed by humic-like chromophores, while phenolic groups react more slowly.

3.8 Environmental implications and limitations

This study emphasizes the critical role of biochar-derived DOM in enhancing Pb(II) adsorption, thereby highlighting its potential to improve biochar's efficiency in heavy metal remediation. A novel approach is introduced, integrating hetero-2DCOS, EEM-PARAFAC, and UV differential log-transformed absorption spectroscopy, to elucidate the binding sequences between DOM's fluorescent chromophores, functional groups, and Pb(II). This integration offers deeper insights into contaminant complexation mechanisms. Kinetic and isothermal adsorption analyses indicate that Pb(II) binding predominantly occurs via chemical interactions, with humic-like components such as C3 showing the strongest affinity for Pb(II). These findings not only enhance our understanding of Pb(II) adsorption mechanisms but also guide the development of more effective biochar-based remediation strategies.

However, it is essential to acknowledge certain limitations in this study. All experiments were conducted under a fixed pH condition (pH 7), which is representative of many natural environments. Nonetheless, pH significantly influences DOM-metal interactions by modulating the protonation state and charge density of functional groups. At low pH, hydrogen bonding and hydrophobic interactions can lead to more compact DOM structures, thereby limiting metal accessibility., In contrast, at high pH, deprotonation of carboxyl and phenolic groups enhances electrostatic attraction and complexation capacity (Xu et al. 2018; Habibul and Chen 2018). Therefore, the binding affinities and structural conformations observed in this study may not fully capture the behavior under more acidic or alkaline conditions. Future studies should consider incorporating a broader range of pH levels to better simulate dynamic environmental conditions.

Moreover, while this study focuses exclusively on the interaction between DOM and Pb(II), it is crucial to acknowledge that natural water and soil environments typically contain multiple heavy metals. These coexisting metals may compete for limited binding sites on DOM, thereby potentially altering the binding behavior observed in single-metal systems. For instance, recent studies have shown that while carboxylic and phenolic groups predominantly bind Pb(II) and Cd(II), nitrogen- and sulfur-containing functional groups exhibit stronger affinities for Cu(II) and Hg(II), respectively (Ye et al. 2025). Such competitive interactions could influence the complexation sequence, mobility, and bioavailability of each metal. Future research should therefore investigate DOM dynamics in multi-metal systems to more accurately reflect environmental conditions and inform remediation approaches.

Importantly, the integrated spectroscopic framework developed in this study provides a powerful tool for examining these limitations. Although it may not fully capture the complexity of molecular interactions and competitive binding behaviors, it offers valuable insights into DOM–metal associations under environmentally relevant conditions. This approach has the potential to

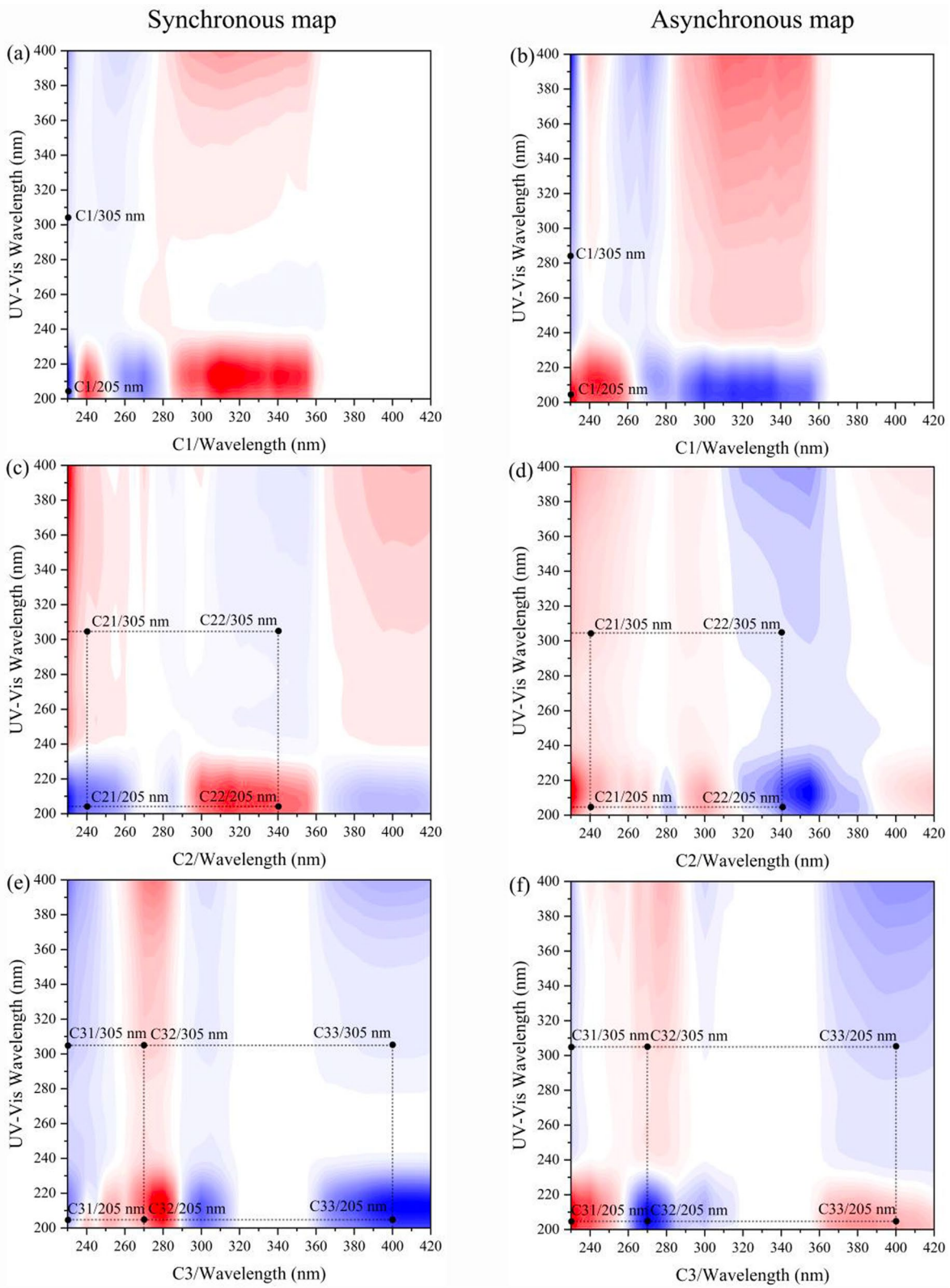

Fig. 8 Synchronous and asynchronous maps obtained via hetero-2DCOS of PARAFAC components and differential log-transformed absorption spectra under Pb(II) concentration perturbation. (Red represents positive correlation, blue represents negative correlation)

enhance our understanding of DOM dynamics in complex systems, thereby supporting more accurate environmental modeling and effective remediation strategies.

4 Conclusion

This study demonstrates that biochar-derived DOM significantly enhances the adsorption capacity of biochar for Pb(II), primarily through chemical interactions, as evidenced by kinetic and isothermal adsorption models (pseudo-second-order, Freundlich, and Temkin). Complementary FTIR and XPS analyses further confirmed the critical roles of oxygen-containing functional groups in Pb(II) binding. The dominant immobilization mechanism was identified as complexation, followed by co-precipitation. The heterogeneity of Pb(II) binding sites within DOM was revealed by differential log-transformed absorption spectra, while EEM-PARAFAC analysis identified three humic-like components, with component C3 (humic-like and tyrosine substances) showing the highest affinity for Pb(II). Hetero-2DCOS analysis further highlighted the rapid reactivity of carboxyl groups in humic-like substances with Pb(II), underscoring their critical role in the adsorption mechanism. These findings suggest that biochar materials enriched with carboxyl groups and humic-like components are highly effective for Pb(II) immobilization, providing a molecular basis for designing targeted remediation strategies. However, it is important to note that this study focuses exclusively on the adsorption behavior of Pb(II), whereas real-world environments often involve the coexistence of multiple heavy metal ions. Future research should investigate the role of DOM in mixed pollutant systems to better understand its interactions under complex environmental conditions. The integration of advanced spectroscopic techniques, particularly hetero-2DCOS combined with EEM-PARAFAC and other spectral methods, is recommended to explore DOM interactions between DOM and a broader range of metal ions and mixed pollutants. Such an approach could deepen our understanding of the complex roles of DOM in environmental systems and facilitate the development of more efficient and sustainable remediation technologies. Although this study provides theoretical support for the application of biochar in Pb(II) pollution remediation, its performance in real-world, complex environments requires further validation through pilot-scale or field experiments. This work not only advances the fundamental knowledge of DOM-metal interactions but also provides practical guidance for optimizing biochar-based strategies in environmental pollution control.

Supplementary Information

The online version contains supplementary material available at https://doi.org/10.1007/s42773-025-00522-7.

Additional file 1.

Acknowledgements

We acknowledge Northeast Agricultural University for providing the support during the experiment. We acknowledge the supports from the National Key R&D Program of China, the Distinguished Youth Science Foundation of Heilongjiang Province, China and the Young Leading Talents Project of Northeast Agricultural University, China.

Author contributions

All authors contributed to the study conception and design. Fuxiang Zhang: Writing – original draft, Resources, Methodology, Validation, Visualization. Boyang Zhou: Writing – original draft, Visualization, Methodology, Investigation, Formal analysis, Data curation. Qiang Fu: Methodology, Conceptualization. Hongliang Jia: Visualization. Yi-Fan Li: Methodology, Conceptualization. Yongzhen Ding: Methodology, Resources, Writing – review & editing. Song Cui: Writing – review & editing, Validation, Supervision, Resources, Conceptualization, Funding acquisition. All authors read and approved the final manuscript.

Funding

This work was supported by the National Key R&D Program of China (2024YFD1501700), the Distinguished Youth Science Foundation of Heilongjiang Province, China (JQ2023E001), and the Young Leading Talents Project of Northeast Agricultural University, China (NEAU2023QNLJ-013, NEAU2024QNLJ-01).

Data availability

All data generated or analyzed during this study are included in this published article and its Additional files.

Declarations

Competing interests

All authors confirm that they have no affiliations with or involvement in any organization or entity with any financial interests or non-financial interest in the subject matter or materials discussed in this manuscript.

Author details

[1]International Joint Research Center for Persistent Toxic Substances (IJRC-PTS), School of Water Conservancy and Civil Engineering, Northeast Agricultural University, Harbin 150030, Heilongjiang, China. [2]Research Center for Eco-Environment Protection of Songhua River Basin, Northeast Agricultural University, Harbin 150030, Heilongjiang, China. [3]IJRC-PTS, College of Environmental Science and Engineering, Dalian Maritime University, Dalian 116026, Liaoning, China. [4]Agro-Environmental Protection Institute, Ministry of Agriculture and Rural Affairs, Tianjin 300191, China.

Received: 5 March 2025 Revised: 6 September 2025 Accepted: 11 September 2025
Published online: 21 October 2025

References

Ahmad M, Rajapaksha AU, Lim JE, Zhang M, Bolan N, Mohan D, Vithanage M, Lee SS, Ok YS (2014) Biochar as a sorbent for contaminant management in soil and water: a review. Chemosphere 99:19–33. https://doi.org/10.1016/j.chemosphere.2013.10.071

Aiken GR, Hsu-Kim H, Ryan JN (2011) Influence of dissolved organic matter on the environmental fate of metals, nanoparticles, and colloids. Environ Sci Technol 45:3196–3201. https://doi.org/10.1021/es103992s

Bai YC, Wu FC, Liu CQ, Li W, Guo JY, Fu PQ, Xing BS, Zheng J (2008) Ultraviolet absorbance titration for determining stability constants of humic

substances with Cu(II) and Hg(II). Anal Chim Acta 616:115–121. https://doi.org/10.1016/j.aca.2008.04.003
Chen J, Gu B, Leboeuf EJ, Pan H, Dai S (2002) Spectroscopic characterization of the structural and functional properties of natural organic matter fractions. Chemosphere 48:59–68. https://doi.org/10.1016/s0045-6535(02)00041-3
Chen W, Habibul N, Liu XY, Sheng GP, Yu HQ (2015) FTIR and synchronous fluorescence heterospectral two-dimensional correlation analyses on the binding characteristics of copper onto dissolved organic matter. Environ Sci Technol 49:2052–2058. https://doi.org/10.1021/es5049495
Chen B, Huang W, Ma S, Feng M, Liu C, Gu X, Chen K (2018) Characterization of chromophoric dissolved organic matter in the littoral zones of eutrophic lakes Taihu and Hongze during the algal bloom season. Water 10:861. https://doi.org/10.3390/w10070861
Chen H, Li W, Wang J, Xu H, Liu Y, Zhang Z, Li Y, Zhang Y (2019) Adsorption of cadmium and lead ions by phosphoric acid-modified biochar generated from chicken feather: selective adsorption and influence of dissolved organic matter. Bioresour Technol 292:121948. https://doi.org/10.1016/j.biortech.2019.121948
Chen YD, Duan XG, Zhang CF, Wang SB, Ren NQ, Ho SH (2020) Graphitic biochar catalysts from anaerobic digestion sludge for nonradical degradation of micropollutants and disinfection. Chem Eng J 384:11. https://doi.org/10.1016/j.cej.2019.123244
Chen H, Yang X, Liu Y, Lin X, Wang J, Zhang Z, Li N, Li Y, Zhang Y (2021) KOH modification effectively enhances the Cd and Pb adsorption performance of N-enriched biochar derived from waste chicken feathers. Waste Manag 130:82–92. https://doi.org/10.1016/j.wasman.2021.05.015
Chen XT, Guo Z, Liu JM, Wu F, Cheng C, Lin H, Ren W, Zhang H (2023) Electron transfer-based peroxydisulfate activation by waste herb residue biochar: Adsorption versus surface oxidation. Chem Eng J 451:12. https://doi.org/10.1016/j.cej.2022.138560
Cui HY, Zhang SB, Zhao MY, Zhao Y, Wei ZM (2020) Parallel faction analysis combined with two-dimensional correlation spectroscopy reveal the characteristics of mercury-composting-derived dissolved organic matter interactions. J Hazard Mater 384:121395. https://doi.org/10.1016/j.jhazmat.2019.121395
Cui S, Lv J, Hough R, Fu Q, Zhang Z, Dong X, Fan X, Li YF (2024) Imidacloprid removal by modified graphitic biochar with Fe/Zn bimetallic oxides. Environ Res 258:119444. https://doi.org/10.1016/j.envres.2024.119444
Dryer DJ, Korshin GV, Fabbricino M (2008) In situ examination of the protonation behavior of fulvic acids using differential absorbance spectroscopy. Environ Sci Technol 42:6644–6649. https://doi.org/10.1021/es800741u
Fan SS, Wang Y, Wang Z, Tang J, Tang J, Li XD (2017) Removal of methylene blue from aqueous solution by sewage sludge-derived biochar: adsorption kinetics, equilibrium, thermodynamics and mechanism. J Environ Chem Eng 5:601–611. https://doi.org/10.1016/j.jece.2016.12.019
Fan QY, Sun JX, Quan GX, Yan JL, Gao JH, Zou XQ, Cui LQ (2020) Insights into the effects of long-term biochar loading on water-soluble organic matter in soil: Implications for the vertical co-migration of heavy metals. Environ Int 136:9. https://doi.org/10.1016/j.envint.2019.105439
Fan XB, Peng LL, Wang XF, Han SQ, Yang LZ, Wang HL, Hao C (2022) Efficient capture of lead ion and methylene blue by functionalized biomass carbon-based adsorbent for wastewater treatment. Ind Crops Prod. https://doi.org/10.1016/j.indcrop.2022.114966
Gao ZY, Guéguen C (2018) Distribution of thiol, humic substances and colored dissolved organic matter during the 2015 Canadian Arctic GEOTRACES cruises. Mar Chem 203:1–9. https://doi.org/10.1016/j.marchem.2018.04.001
Guo XJ, Peng YY, Li NX, Tian YY, Dai LC, Wu Y, Huang Y (2022) Effect of biochar-derived DOM on the interaction between Cu(II) and biochar prepared at different pyrolysis temperatures. J Hazard Mater 421:126739. https://doi.org/10.1016/j.jhazmat.2021.126739
Habibul N, Chen W (2018) Structural response of humic acid upon binding with lead: a spectroscopic insight. Sci Total Environ 643:479–485. https://doi.org/10.1016/j.scitotenv.2018.06.229
Hameed R, Li G, Son Y, Fang H, Kim T, Zhu C, Feng Y, Zhang L, Abbas A, Zhao X, Wang J, Li J, Dai Z, Du D (2023) Structural characteristics of dissolved black carbon and its interactions with organic and inorganic contaminants: a critical review. Sci Total Environ 872:162210. https://doi.org/10.1016/j.scitotenv.2023.162210
He B, Yun Z, Shi J, Jiang G (2012) Research progress of heavy metal pollution in China: sources, analytical methods, status, and toxicity. Chin Sci Bull 58:134–140. https://doi.org/10.1007/s11434-012-5541-0
He CJ, He XW, Li JJ, Luo Y, Li JC, Pei Y, Jiang JY (2021) The spectral characteristics of biochar-derived dissolved organic matter at different pyrolysis temperatures. J Environ Chem Eng 9:9. https://doi.org/10.1016/j.jece.2021.106075
Hou JW, Liu DP, Wu FC, Gao HJ, Yu HB (2023) Applying synchronous fluorescence spectroscopy combined with Gaussian band fitting and two-dimensional correlation to characterize interactions of copper (II) with dissolved organic matter from urban river sediments. J Environ Chem Eng 11:110038. https://doi.org/10.1016/j.jece.2023.110038
Hou EY, Jia XY, Wang LW, Mcgrath SP, Zhu YG, Hu Q, Zhao FJ, Bank MS, O'Connor D, Nriagu J (2025) Global soil pollution by toxic metals threatens agriculture and human health. Science. https://doi.org/10.1126/science.adr5214
Huang M, Li ZW, Huang B, Luo NL, Zhang Q, Zhai XQ, Zeng GM (2018) Investigating binding characteristics of cadmium and copper to DOM derived from compost and rice straw using EEM-PARAFAC combined with two-dimensional FTIR correlation analyses. J Hazard Mater 344:539–548. https://doi.org/10.1016/j.jhazmat.2017.10.022
Huang M, Li Z, Chen M, Wen J, Luo N, Xu W, Ding X, Xing W (2020) Dissolved organic matter released from rice straw and straw biochar: contrasting molecular composition and lead binding behaviors. Sci Total Environ 739:140378. https://doi.org/10.1016/j.scitotenv.2020.140378
Hur J, Lee BM (2011) Characterization of binding site heterogeneity for copper within dissolved organic matter fractions using two-dimensional correlation fluorescence spectroscopy. Chemosphere 83:1603–1611. https://doi.org/10.1016/j.chemosphere.2011.01.004
Janot N, Reiller PE, Korshin GV, Benedetti MF (2010) Using spectrophotometric titrations to characterize Humic acid reactivity at environmental concentrations. Environ Sci Technol 44:6782–6788. https://doi.org/10.1021/es1012142
Jiang S, Dai G, Liu Z, He T, Zhong J, Ma Y, Shu Y (2022) Field-scale fluorescence fingerprints of biochar-derived dissolved organic matter (DOM) provide an effective way to trace biochar migration and the downward co-migration of Pb, Cu and As in soil. Chemosphere 301:134738. https://doi.org/10.1016/j.chemosphere.2022.134738
Ke YX, Zhang FX, Zhang ZL, Hough R, Fu Q, Li YF, Cui S (2023) Effect of combined aging treatment on biochar adsorption and speciation distribution for Cd(II). Sci Total Environ 867:10. https://doi.org/10.1016/j.scitotenv.2023.161593
Lawaetz AJ, Stedmon CA (2009) Fluorescence intensity calibration using the Raman scatter peak of water. Appl Spectrosc 63:936–940. https://doi.org/10.1366/000370209788964548
Li Z, Ma Z, van der Kuijp TJ, Yuan Z, Huang L (2014) A review of soil heavy metal pollution from mines in China: pollution and health risk assessment. Sci Total Environ 468:843–853. https://doi.org/10.1016/j.scitotenv.2013.08.090
Li M, Zhang AF, Wu HM, Liu H, Lv JL (2017) Predicting potential release of dissolved organic matter from biochars derived from agricultural residues using fluorescence and ultraviolet absorbance. J Hazard Mater 334:86–92. https://doi.org/10.1016/j.jhazmat.2017.03.064
Li C, Wang Q, Lai Z, Mu J (2024a) One-step synthesis of novel nitrogen-doped biochar from N-rich waste straw particleboard for efficient Pb(II) adsorption. Microchem J. https://doi.org/10.1016/j.microc.2024.112206
Li HY, Wang J, Zhu XJ (2024b) Adsorption of Pb(II) and Ag(I) using iron/manganese oxides modification biochar. Ind Crops Prod 215:11. https://doi.org/10.1016/j.indcrop.2024.118615
Liu YX, Lonappan L, Brar SK, Yang SM (2018) Impact of biochar amendment in agricultural soils on the sorption, desorption, and degradation of pesticides: a review. Sci Total Environ 645:60–70. https://doi.org/10.1016/j.scitotenv.2018.07.099
Liu D, Gao H, Yu H, Song Y (2022) Applying eem-parafac combined with moving-window 2dcos and structural equation modeling to characterize binding properties of Cu (II) with DOM from different sources in an urbanized river. Water Res 227:119317. https://doi.org/10.1016/j.watres.2022.119317
Lou YM, Joseph S, Li LQ, Graber ER, Liu XY, Pan GX (2016) Water extract from straw biochar used for plant growth promotion: an initial test. BioResources 11:249–266

Lu Y, Yan M, Korshin GV (2017) Spectroscopic study of interactions of lead (II) ions with dissolved organic matter: evidence of preferential engagement of carboxylic groups. Geochim Cosmochim Acta 213:308–316. https://doi.org/10.1016/j.gca.2017.06.014

Mohan D, Sarswat A, Ok YS, Pittman CU (2014) Organic and inorganic contaminants removal from water with biochar, a renewable, low cost and sustainable adsorbent - a critical review. Bioresour Technol 160:191–202. https://doi.org/10.1016/j.biortech.2014.01.120

Murphy KR, Stedmon CA, Wenig P, Bro R (2014) OpenFluor– an online spectral library of auto-fluorescence by organic compounds in the environment. Anal Methods 6:658–661. https://doi.org/10.1039/c3ay41935e

Nazari S, Rahimi G, Nezhad AKJ (2019) Effectiveness of native and citric acid-enriched biochar of Chickpea straw in Cd and Pb sorption in an acidic soil. J Environ Chem Eng 7:6. https://doi.org/10.1016/j.jece.2019.103064

Noda I (2016) Techniques useful in two-dimensional correlation and codistribution spectroscopy (2DCOS and 2DCDS) analyses. J Mol Struct 1124:29–41. https://doi.org/10.1016/j.molstruc.2016.01.089

Noda, I., Ozaki, Y, (2005). Two-dimensional Correlation Spectroscopy: Applications in Vibrational and Optical Spectroscopy. John Wiley & Sons.

Romero CM, Engel RE, D'Andrilli J, Miller PR, Wallander R (2019) Compositional tracking of dissolved organic matter in semiarid wheat-based cropping systems using fluorescence EEMs-PARAFAC and absorbance spectroscopy. J Arid Environ 167:34–42. https://doi.org/10.1016/j.jaridenv.2019.04.013

Sebastian A, Nangia A, Prasad MNV (2019) Cadmium and sodium adsorption properties of magnetite nanoparticles synthesized from *Hevea brasiliensis* Muell. Arg. bark: relevance in amelioration of metal stress in rice. J Hazard Mater 371:261–272. https://doi.org/10.1016/j.jhazmat.2019.03.021

Shu Y, Kong F, He Y, Chen L, Liu H, Zan F, Lu X, Wu T, Si D, Mao J, Wu X (2024) Machine learning-assisted source tracing in domestic-industrial wastewater: A fluorescence information-based approach. Water Res 268:122618. https://doi.org/10.1016/j.watres.2024.122618

Sondergaard M, Stedmon CA, Borch NH (2003) Fate of terrigenous dissolved organic matter (DOM) in estuaries: aggregation and bioavailability. Ophelia 57:161–176. https://doi.org/10.1080/00785236.2003.10409512

Tan X, Liu Y, Zeng G, Wang X, Hu X, Gu Y, Yang Z (2015) Application of biochar for the removal of pollutants from aqueous solutions. Chemosphere 125:70–85. https://doi.org/10.1016/j.chemosphere.2014.12.058

Tian XS, Chu SY, Hu YJ, Luo LZ, Lin XA, Wang H (2025) Removal of heavy metals from single- and multi-metal solution by magnetic microalgae-derived biochar. J Water Process Eng 69:11. https://doi.org/10.1016/j.jwpe.2024.106622

Wan Z, Xu Z, Sun Y, He M, Hou D, Cao X, Tsang DCW (2021) Critical impact of nitrogen vacancies in nonradical carbocatalysis on nitrogen-doped graphitic biochar. Environ Sci Technol 55:7004–7014. https://doi.org/10.1021/acs.est.0c08531

Wang Y, Wang L, Li ZT, Yang D, Xu JM, Liu XM (2021) MgO-laden biochar enhances the immobilization of Cd/Pb in aqueous solution and contaminated soil. Biochar 3:175–188. https://doi.org/10.1007/s42773-020-00080-0

Wang Y, Li J, Xu L, Xu Q, Wu D, Ai Y, Li D, Liu W, Qu J, Wang L, Zhang Y (2023) The effect and spectral response mechanism of dissolved organic matter (DOM) in Pb(II) adsorption onto biochar. J Environ Chem Eng 11:111115. https://doi.org/10.1016/j.jece.2023.111115

Wang M, Zhu Y, Yue C, Ge H, Yan J, Yang Y, Quan G (2024) Preparation of a novel magnetic calcium-based biochar for arsenic removal: behavior and dominant mechanism. Sep Purif Technol 336:126384. https://doi.org/10.1016/j.seppur.2024.126384

Xing J, Xu G, Li G (2020) Analysis of the complexation behaviors of Cu(II) with DOM from sludge-based biochars and agricultural soil: effect of pyrolysis temperature. Chemosphere 250:126184. https://doi.org/10.1016/j.chemosphere.2020.126184

Xu H, Yan M, Li W, Jiang H, Guo L (2018) Dissolved organic matter binding with Pb(II) as characterized by differential spectra and 2D UV-FTIR heterospectral correlation analysis. Water Res 144:435–443. https://doi.org/10.1016/j.watres.2018.07.062

Xu W, Jin Y, Zeng G (2024) Introduction of heavy metals contamination in the water and soil: a review on source, toxicity and remediation methods. Green Chem Lett Rev 17:2404235. https://doi.org/10.1080/17518253.2024.2404235

Yamashita Y, Jaffé R (2008) Characterizing the interactions between trace metals and dissolved organic matter using excitation-emission matrix and parallel factor analysis. Environ Sci Technol 42:7374–7379. https://doi.org/10.1021/es801357h

Yan MQ, Wang DS, Korshin GV, Benedetti MF (2013) Quantifying metal ions binding onto dissolved organic matter using log-transformed absorbance spectra. Water Res 47:2603–2611. https://doi.org/10.1016/j.watres.2013.02.044

Yan CX, Wang WY, Nie MH, Ding MJ, Wang P, Zhang H, Huang GX (2023) Characterization of copper binding to biochar-derived dissolved organic matter: effects of pyrolysis temperature and natural wetland plants. J Hazard Mater 442:13. https://doi.org/10.1016/j.jhazmat.2022.130076

Yang YK, Luo X, Zhang J, Ma XK, Sun PZ, Zhao L (2022) Sewage sludge-coconut fiber co-pyrolysis biochar: mechanisms underlying synergistic heavy metal stabilization and ciprofloxacin adsorption. J Cleaner Prod 375:10. https://doi.org/10.1016/j.jclepro.2022.134149

Yang W, Lu C, Liang B, Yin C, Lei G, Wang B, Zhou X, Zhen J, Quan S, Jing Y (2023) Removal of Pb(II) from aqueous solution and adsorption kinetics of corn stalk biochar. Separations 10:438. https://doi.org/10.3390/separations10080438

Ye QT, Wang P, Liang YZ, Li R, Shi ZQ (2025) Modeling the equilibrium and kinetics of heavy metals reactions with dissolved organic matter. Appl Geochem 181:11. https://doi.org/10.1016/j.apgeochem.2025.106300

Yue X, Chen X, Kang J, Xu Y, Zhang H (2025) Insight into the efficacy and mechanism of persulfate activation using KHCO3 modified biochar: the overlooked contribution of adsorption. Chem Eng J 516:163781. https://doi.org/10.1016/j.cej.2025.163781

Zeng Z, Zheng P, Ding AQ, Zhang M, Abbas G, Li W (2017) Source analysis of organic matter in swine wastewater after anaerobic digestion with EEM-PARAFAC. Environ Sci Pollut Res 24:6770–6778. https://doi.org/10.1007/s11356-016-8324-3

Zhang XY, Su C, Liu XY, Liu ZG, Gu PX, Deng M, Liu Q (2020) Periodical changes of dissolved organic matter (DOM) properties induced by biochar application and its impact on downward migration of heavy metals under flood conditions. J Cleaner Prod 275:123787. https://doi.org/10.1016/j.jclepro.2020.123787

Zhang XL, Cai XW, Wang ZW, Yang X, Li S, Liang GW, Xie XY (2021) Insight into metal binding properties of biochar-derived DOM using EEM-PARAFAC and differential absorption spectra combined with two-dimensional correlation spectroscopy. Environ Sci Pollut Res 28:13375–13393. https://doi.org/10.1007/s11356-020-11573-7

Zhang JL, Peng YT, Liu TZ, Wang ZH (2025) Na related nanowhisker-containing biochar obtained from self-catalyzation and functionalization of papermaking black liquor lignin with superior heavy metal immobilization capability. Bioresour Technol 417:13. https://doi.org/10.1016/j.biortech.2024.131866

Zhou X, Zhao C, Sun J, Cao Y, Yao K, Xu M (2023) A deep learning method for predicting lead content in oilseed rape leaves using fluorescence hyperspectral imaging. Food Chem 409:135251. https://doi.org/10.1016/j.foodchem.2022.135251